Natural image synthesis for the retina with variational information bottleneck representation

Anonymous Author(s)
Affiliation
Address
email

Abstract

Visual prostheses provide artificial vision to the blind by encoding the natural visual scene onto electrical signals that stimulate the undamaged neurons in the retina. Encoding the high-dimensional visual input onto the limited number of electrodes of the prosthesis results in unnatural perceptions that often induces users to avoid using the device due to the very high cognitive burden. But, even in the unimpaired natural visual system, is all the visual scene information required to explain the neuronal responses? In this work, we search for answers to this question by developing a joint model of the natural visual input and neuronal responses using the Information Bottleneck (IB) framework that is able to represent features of the input data into a few latent variables that play a role in the prediction of the outputs. The correlations between data samples, acquired from published experiments on ex-vivo retinas, is accounted for in the model by a Gaussian Process (GP) prior. The proposed IB-GP model performs competitive to the state-of-the-art feedforward convolutional networks in prediction of spike responses to natural stimuli. We observe that reconstructed stimuli from latent variables show robustness in spike prediction across models. Finally, the IB-GP model is used in a closed loop iterative process to obtain reduced-complexity inputs that elicit responses as those elicited by the original stimuli.

1 Introduction

A fundamental challenge in neuroprosthetics is finding the proper input to a sensory or motor system that yields a desired functional output. This is achieved naturally by the underlying physiological circuit in an unimpaired system. For example, in the vision system, when an image is formed onto the photoreceptors, the electrical neural activity is processed by several layers of neurons within the retina, and a train of electrical neural spikes is sent to the visual cortex via the optic nerve producing a perception of the visual scene. Retinal degenerative diseases may break this flow of information at one point while the rest of the circuit remains intact [24] [22]. In this case, prostheses could be used to artificially stimulate neural cells in the retina to restore the lost functionality [38] [20] [16]. The current technology in the visual prosthesis consists of an array of stimulating electrodes. The number of stimulating electrodes is $\sim$4 orders of magnitude smaller than the number of photoreceptors [15]. Given this fact, one can ask: even in the natural vision system, is it possible to reduce the complexity of the input stimuli and still obtain the same functional behavior? In other words, what are the reduced spatiotemporal stimuli that elicit the same response as that of the higher-dimensional original input?

Nirenberg et al. [26] showed that a good encoder of the retina responses dramatically increases the prosthesis performance. In this work, we focus on the *natural* vision system and search for answers to these questions. Our system consists of the spatiotemporal stimuli impinging on the photoreceptors in the retina up to the spiking responses emitted by the Retinal Ganglion Cells (RGCs). Linear-nonlinear

Submitted to 36th Conference on Neural Information Processing Systems (NeurIPS 2022). Do not distribute.

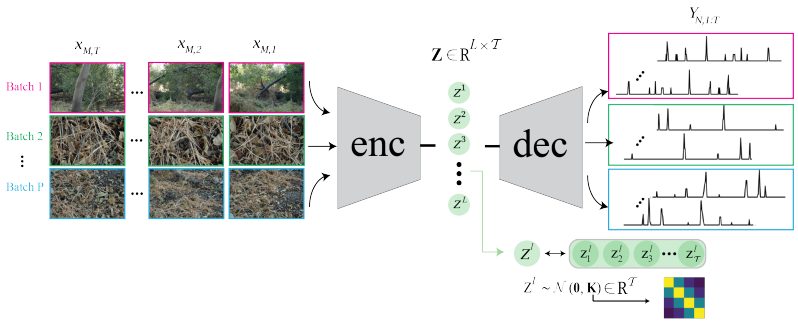

Figure 1: Overview of the IB-GP model of the retina responses. Batches of T high-dimensional stimuli are encoded into a low-dimensional space and decoded to the N neuronal response trains of length T. The latent space consists of L latent vectors. Each latent vector z^l is modeled by a GP prior to account for the sample correlations in the original space.

(LN) [11] and generalized linear models (GLMs) [28] [29] were proposed for encoding of the retinal neural codes. Although successful for artificial stimuli such as white noise, they could not faithfully describe RGCs responses to natural stimuli [17]. The convolutional neural network (CNN) model of McIntosh et al. [25] was the first model capable of such computation. This was followed by other efforts such as employing recurrent neural networks [5] or variants of CNNs [23]. Although high-dimensional in nature, neural activity can be well explained by low-dimensional representations [12] [14] [31]. This opens up the possibility of using models that learn a latent representation of data, such as VAEs [18] and ICAs [21]. Accordingly, latent dynamical methods that inspect sources of low-dimensional structure in the neural response have recently gained growing interest [19] [37].

Inspired by the Deep Variational Information Bottleneck (DVIB) [2] [9], we introduce the Information Bottleneck Gaussian Process (IB-GP), a latent space model that can extract the principal features of the *joint* stimuli-responses distribution that are sufficient for predicting the retina responses. The schematic of the IB-GP is depicted in Fig. 1. This model is a variational approximation to the original Information Bottleneck framework of Tishby et al. [34]. The objective of IB is to obtain a reduced representation of the input source that preserves maximum information about the output response. DVIB assumes the IB's latent codes are i.i.d. This is a poor assumption for the retina dataset. The reason for this is two-fold. First, while observing a scene, images captured by the retina are naturally very similar. Second, during fixation, the eyes undergo dynamic movements that shift the gaze's center. Therefore, incorporating the temporal correlations among data samples should provide a better model. Accordingly, IB-GP uses a Gaussian Process prior to modeling the retina dataset. Our contributions in this work are:

- **A probabilistic model**: We propose IB-GP, a new model for the RGCs spike train in response to the complex natural visual stimuli using the IB framework. The model integrates a GP prior into the IB latent code that can learn the temporal dynamics of the data in a lower dimension space. This model shows favorable performance compared to the state-of-the-art feedforward CNN models of the retina tested on real-world experimental data.

- **Latent dynamics analysis**: We analyze the latent space of the proposed model and extract low-dimensional dynamics consistent with the high-dimensional data dynamics. We show that the extracted dynamics are more predictive of the neural responses compared to dynamics extracted by a model with no temporal prior constraint.

- **Closed loop image synthesis**: Utilizing the IB-GP model, which only allows principal features of the input stimuli to pass the bottleneck, the original input stimuli are pruned to contain the minimum information required for producing the RGC responses. The resulting reduced-dimension optimized stimuli could be used for the next round of measurements in an iterative process.

In the following, we start by reviewing the related work in section 2, the general setting of the problem and our model are presented in section 3, and the closed-loop stimuli optimization procedure is

outlined in section 4. Experiments and results are presented in sections 5 and 6[1]. Finally, the results are discussed in section 7.

2 Related work

In the RGC modeling literature, our work is the closest to the work of McIntosh et al. [25] in which a CNN is used to model the responses of RGCs to a set of input stimuli. Despite the simplicity of this approach, the CNN cannot be directly utilized to extract the principal features of the stimuli contributing to the neural responses. On the other hand, neural latent models such as [19] [27] [32] are primarily applied to cortical recordings to learn sources of neural variability in the motor cortex data. Unlike our model, which directly relates the stimuli to the neural responses, the stimuli in those lines of work are utilized as a guide star to disentangle the latent factors. Therefore, these methods are not directly applicable to modeling the RGC responses to input stimuli.

In the closed-loop physical system input optimization literature, our work is related to [30][33][36][4]. In particular, for neuroscience applications, authors in [4] control the activity of the individual neuronal sites in V4 by optimizing individual input stimulation, whereas in our work, thanks to the learned latent code of the entire population of the targeted neurons, all stimuli are optimized together.

In the work of Shah et al. [33], the RGCs responses to electrical stimulation were optimized by first developing a model for the electrical stimuli and the spiking probabilities and then using the model for adaptive stimulation. The model is obtained by parameterizing the spike amplitude and electrical stimulation threshold by a few parameters and then maximizing an evident lower bound on the spiking probabilities. Our work does not assume any relevant relation between the input stimuli and the spiking probabilities. Instead, the relevant parts of the input for predicting the output are discovered automatically.

3 Methods

3.1 IB-GP model

Notation and problem formulation The input stimuli dataset $\mathbf{X} \in \mathbb{R}^{M\times T}$ consists of T consecutive spatial inputs of size M, i.e. $\mathbf{X} = [x_{M,1}, x_{M,2}, \cdots, x_{M,T}]$, that are projected in the retina at a constant rate to elicit count responses of the form $\mathbf{Y} \in \mathbb{N}^{N\times T}$, where $\mathbf{Y} = [y_{N,1}, y_{N,2}, \cdots, y_{N,T}]$ and N denotes the number of RGCs. With the above assumptions, we formulate the problem as finding the latent variables $\mathbf{Z} \in \mathbb{R}^{L\times\mathcal{T}}$ that have maximal mutual information $I(\mathbf{Z}, \mathbf{Y})$ with targets $\mathbf{Y}$. We note that $\mathbf{Z}$ is comprised of $\mathcal{T}$ consecutive data points, i.e. $\mathbf{Z} = [z_{L,1}, z_{L,2}, \cdots, z_{L,\mathcal{T}}]$ where $\mathcal{T} \leq T$. $\mathbf{Z}$ is simultaneously constrained to have minimal mutual information with $\mathbf{X}$. Therefore, the constraint optimization problem can be written as

$$\mathcal{L}_{IB} = \max_{\zeta} \big[\, I_{IB}\big]$$

where

$$I_{IB} = I(\mathbf{Z}, \mathbf{Y}; \zeta) - \beta I(\mathbf{Z}, \mathbf{X}; \zeta)\ . \tag{1}$$

ζ designates the parameters of the model (notation henceforth dropped for brevity) and β is a variable to adjust the amount of reduced and preserved information in $\mathbf{Z}$. To obtain these latent variables, we approximate their posterior distribution with a parametric stochastic encoder $p_\phi(\mathbf{Z}|\mathbf{X})$. Due to the *spatio-temporal* nature of the data, assumption of data independence along the time dimension is not valid. The same is true in the latent space. To account for this fact, we assume a posterior of the form:

$$p_\phi(\mathbf{Z}|\mathbf{X}) = \prod_{l=1}^{L} \mathcal{N}(\mathbf{z}^l | \boldsymbol{\mu}_\phi^l(\mathbf{X}), \boldsymbol{\Sigma}_\phi^l(\mathbf{X})) \tag{2}$$

where $\mathbf{z}^l$ denotes the l-th latent vector of size $\mathcal{T}$. In Eq. 2, $\boldsymbol{\mu}_\phi^l \in \mathbb{R}^{\mathcal{T}}$ and $\boldsymbol{\Sigma}_\phi^l \in \mathbb{R}^{\mathcal{T}\times\mathcal{T}}$ are the mean and covariance matrix of a multi-variate normal distribution that are functions of the inputs. We choose the structure of the covariance of the multivariate normal distribution in Eq. 2 to reflect the

[1] Code and data for reproducing the results are provided in the Appendix 11.

time correlations in the data. Hence, similar to previous work [3] [7] [13], we construct the $\mathbf{\Sigma}_\phi^l$ in our model by the product of bidiagonal matrices:

$$[\mathbf{\Sigma}_\phi^l]^{-1} = \mathbf{V}_l^{\mathrm{T}}\mathbf{V}_l + \mathbf{I} \text{ where } [\mathbf{V}_l]_{\tau\tau\prime} = \begin{cases} v_{\tau\tau\prime}^l & \tau\prime \in \{\tau, \tau+1\} \\ 0 & \text{o.w.} \end{cases} \tag{3}$$

We note that the low-rank GP kernel assumption makes the computation required for drawing samples from p_ϕ linear in time [3]. Expanding the IB objective in Eq. 1 (details in the Appendix 1), we have:

$$I_{IB} = \int d\mathbf{Y}\, d\mathbf{Z}\, p(\mathbf{Y}, \mathbf{Z})\, \log \frac{p(\mathbf{Y}|\mathbf{Z})}{p(\mathbf{Y})} - \beta \int d\mathbf{X}\, d\mathbf{Z}\, p(\mathbf{X}, \mathbf{Z})\, \log \frac{p_\phi(\mathbf{Z}|\mathbf{X})}{p(\mathbf{Z})} \tag{4}$$

Although all terms in the RHS of Eq. 4 are fully defined, computing marginal distributions $p(\mathbf{Z})$ and $p(\mathbf{Y}|\mathbf{Z})$ may be intractable. We use a variational approximation for $p(\mathbf{Y}|\mathbf{Z})$ that is parameterized with θ. On the other hand, the prior on the latent variables, i.e. $p(\mathbf{Z})$, is modeled using GPs. In particular, we assume a GP prior on $\mathbf{Z}$ defined as a multivariate normal:

$$\rho(\mathbf{Z}) = \prod_{l=1}^{L} \mathcal{N}(\mathbf{z}^l|\mathbf{0}, \mathbf{K}) \tag{5}$$

where ρ is the variational approximation for the prior and $\mathbf{K}$ is the covariance function that models the temporal correlations in the latent space. In more details, the covariance between the τ-th and the $\tau\prime$-th samples is computed as $\mathbf{K}_{\tau\tau\prime} = \mathcal{K}(\tau, \tau\prime)$ where $\mathcal{K}$ is the kernel function. We used the Cauchy kernel:

$$\mathcal{K}(\tau, \tau\prime) = \sigma^2 \big(1 + \frac{(\tau - \tau\prime)^2}{l^2}\big)^{-1} \tag{6}$$

where σ and l are the magnitude and temporal scales of the kernel function, respectively. Cauchy kernels have proved successful in modeling of the time-series systems with multi-scale dynamics as shown before [13]. Substituting the variational approximations of the intractable marginals in Eq. 4 and using the fact that the Kullback Leibler (KL) divergence is always positive, we obtain a lower bound for the IB objective:

$$I_{IB} \approx \frac{1}{T} \sum_{t=1}^{T} \Big[\mathbb{E}_{p_\phi(\mathbf{Z}|x_{1:\tau(t)})}[\log q_\theta(y_t|\mathbf{Z})] - \beta D_{KL}[p_\phi(\mathbf{Z}|x_{1:\tau(t)})||\rho(\mathbf{Z})] \Big] . \tag{7}$$

where $\tau(t)$ is to represent time dependence up to time t. See Appendix 1 for more details.

3.2 Other models considered

Maximum likelihood feedforward CNN is used as a comparison baseline. We use the same CNN network that was shown in the previous work to obtain state-of-the-art results on a larger version of the *Natural* dataset [25]. The predicted outputs of the network are the averaged maximum likelihood estimation of the retina responses given the input stimuli. Artificial noise is injected into the model during optimization to account for the variability in retinal spiking.

IB-Disjoint optimizes the objective from Eq. 7 using the same training procedure as that of the original method. The difference lies in that the IB-Disjoint assumes latent samples are temporally independent. Accordingly, an isometric Gaussian distribution is employed as the prior in Eq. 7. This model is akin to the standard Variational Auto-encoder [18], or vanilla DVIB [2] in which samples in the data and latent space are assumed to be independent (no latent GP).

4 Closed loop stimulation

In this section, we take advantage of the model developed in the previous sections to devise an algorithm that uses the prior recorded data to optimize the stimulation by iteration in subsequent measurements in a closed loop. Specifically, we assume the latent variables of the learned model, henceforth referred to as the *forward model*, have captured the principal rules governing the underlying biological system. We intend to find a transformed version of the original input stimuli that yields a

set of latent variables that produce the most correlated responses with the original target responses in the subsequent round of measurements. Of course, the original stimuli themselves are one set of solutions. However, this is not a useful transformation. Instead, we are interested in obtaining the best transformation subject to a constraint on their complexity. Hence, we define a parametric function $f_\xi : \mathbb{R}^{M\times T} \to \mathbb{R}^{M\times T}$ that maps the complex original stimuli $\mathbf{X}$ onto the transformed stimuli $\mathbf{X}^*$. Passing $\mathbf{X}^*$ to the forward model, the parameter of the mapping functions, i.e. ξ, are optimized so that the forward model's output responses $\mathbf{Y}^*$ are the most correlated with the original responses $\mathbf{Y}$. Denoting the original stimuli and responses as $\mathbf{X}^{\text{orig}} := \mathbf{X}$ and $\mathbf{Y}^{\text{orig}} := \mathbf{Y}$, the objective function reads as:

$$\min_{\xi} \; D_1(\mathbf{Y}^{\text{orig}}, \mathbf{Y}^*) + \alpha\big[D_2(\mathbf{X}^{\text{orig}}, \mathbf{X}^*) + D_3(\mathbf{X}^*)\big]$$

where:

$$\mathbf{X}^* = f_\xi(\mathbf{X}^{\text{orig}}),\; \mathbf{Z}^* \sim p_\phi(.|\mathbf{X}^*),\; \mathbf{Y}^* \sim q_\theta(.|\mathbf{Z}^*). \tag{8}$$

Therein, p_ϕ and q_θ are the encoder and decoder of the forward model trained on the prior data. D_1 is a measure to ensure the closeness of the original target outputs and the responses of the forward model to $\mathbf{X}^*$. D_2 is a similarity measure between the original and synthesized stimuli $\mathbf{X}^{\text{orig}}$ and $\mathbf{X}^*$ which encourages the image synthesizer to focus on finding the essential features in the stimuli rather than synthesizing entirely new solutions. Finally, D_3 is used to constrain the synthesized stimuli $\mathbf{X}^*$ to be smooth. Contributions of D_2 and D_3 to the total loss in Eq. 8 are tuned by hyperparameter α. Two major mechanisms help to prevent f_ξ from being simply an identity mapping. One, during the training of the f_ξ, the encoder's latent variables $\mathbf{Z}^*$ are masked by zeroing out all the latent variables except for the most informative one. This way, $\mathbf{X}^{\text{orig}}$ is no longer the optimal solution that minimizes the first term in the objective function. Two, f_ξ is implemented using an Autoencoder architecture with a limited latent capacity. Finally, the optimized stimuli for subsequent rounds of measurements can be obtained by the following procedure: (1) map the original stimuli to the optimized stimuli using mapping f_ξ, (2) encode the new input $\mathbf{X}^*$ to the posterior $\mathbf{Z}^*$, (3) decode the latent variables, (4) construct the metric D and backpropagate the error to fit f_ξ, (5) once converged, use the mapping function to obtain the optimized stimuli $\mathbf{X}^*$ (6) send new inputs $\mathbf{X}^*$ to the true biological system (or its model) and observe the new true system outputs, (7) to repeat the procedure, use the true system's new inputs and outputs to fine-tune the forward model and (8) repeat.

5 Experiments

5.1 Dataset

We focus on applying our model to the time-series dataset containing the 2D train of input stimuli (images) entering the vision circuit of an example subject and the corresponding elicited count responses of a group of neurons. Specifically, we use two real-world experimental datasets. The first one, *Natural* dataset, contains natural scene images as input stimuli and spike trains from nine RGCs in Salamander [25] [2]. The second dataset, *Brownian-movement*, is a public dataset which contains images with disc-like shapes having Brownian movements and the spike trains elicited in 91 Rat's RGCs [8].

5.2 Forward modeling

Training specifications We used the models outlined in section 3 to fit the neural activities and input stimuli. The Natural dataset contains 359000 input-output samples in the training set, of which 20% was randomly chosen for validation. The test set contains 5000 averaged repeated trials of novel stimuli. We note that the output responses were first binned at 10 ms and then smoothed using a Gaussian filter with a standard deviation equal to the bin size. The Brownian-movement dataset contains 129600 pairs of input images and output spikes binned at 12.5 ms in the training set, of which 20% was randomly chosen for validation. The test set contains 1800 novel stimuli. We varied the number of neurons in the Brownian dataset for which we tested our model. We report the results for nine neurons in the main paper and 15, 21, 27, and 36 neurons in Appendix 6.

[2] The Natural dataset, which has been made available and is used in this work, is a subset of the original dataset of [25] that was provided by the authors therein. This dataset contained responses of only nine RGCs.

Models and evaluation metrics To account for the discrete nature of the output responses (count time series), we employ a Poisson regression model for both IB-GP and IB-Disjoint decoder as well as the feedforward CNN loss term, i.e. $q_\theta(y_t|\mathbf{Z}) = \text{Po}(y_t|f_\theta(\mathbf{Z}))$ where f_θ is the parametric network. We sweep the number of latent factors and the prior pressure constraint β for both IB-GP and IB-Disjoint. For the Natural and Brownian datasets, the number of latents is swept between 1 to 15 and 1 to 50 variables, respectively. Except for the latent space of the IB-GP, which requires more variables to model its covariance matrix, IB-GP and IB-Disjoint are implemented using the same architectures. All hyperparameters in the training of the two models are fixed to be the same. The architectures of the networks and the training setup are explained in more detail in Appendix 3. We perform a three-fold fitting of the models for the spike prediction results. We report the models' Poisson negative log-likelihoods on the ground truth data. Moreover, we use the Pearson Correlation [6] between the ground truth data and the networks' prediction as another metric for evaluating the performance of the models.

Traversal analysis We perform traversal analysis on the latent space of IB-GP and IB-Disjoint models to study the amount of information picked by each latent variable. To this end, the encoder $p_\phi(\mathbf{Z}|\mathbf{X})$ is fed with a batch of input stimuli to initialize the latents. In the IB-GP model, the l-th latent is sampled from $\mathcal{N}(\mathbf{0}, m\mathbf{K})$ where m is a multiplier that is traversed in the range $[-3, 3]$ while keeping all the other latents to their inferred values. The latent variables in the IB-Disjoint model are sampled similarly but from the normal univariate distribution $\mathcal{N}(\mathbf{0}, m\mathbf{I})$. The latents are then passed to the decoder that reconstructs the output responses. The output responses of the traversed model are then compared against the non-traversed responses.

5.3 Closed-loop image synthesis

We use both the IB-GP and IB-Disjoint with a latent size of 4. The prior constraint parameter β is set to 0.05. These hyperparameters are chosen as a trade-off between the latent space compression and RGCs neural activity fitting accuracy. The image synthesizer f_ξ is implemented using an Autoencoder architecture [35] with a latent size of 15. The rationale for this choice of architecture is explained in Appendix 3. To allow for multi-phase iterative optimization, we use a neural network as the proxy for the true biological system trained on the Natural dataset. This model is trained once and kept fixed. We use the feedforward CNN network of McIntosh et al. [25] as the true model in order to rule out the possibility of obtaining correlated responses due to the similarity of the IB-GP model and the true model. We optimize the stimuli in a three-phase closed-loop experiment. We used the Poisson regression loss as the D_1 measure in the objective function 8. The similarity measure D_2 between the synthesized and original stimuli is computed using a Mean Squared Error (MSE). Total Variation (TV) metric [10] is used as the D_3 measure. We analyze the contributions of all measures to the quality of the synthesized stimuli by sweeping the hyperparameter α.

6 Results

6.1 Forward modeling

RGC neural activity fitting Performances of the IB-GP, IB-Disjoint, and Feedforward CNN in fittings to neural activities versus the number of latents for both Natural and Brownian datasets are plotted in Figure 2. Figure 2a-d shows that IB-GP outperforms IB-Disjoint almost in all cases. For a fixed β value, the performance of the IB-Disjoint gets closer to that of the IB-GP with the increase in the number of latents. This indicates that IB-GP learns neural activities with a fewer number of latents. Similar is the case with β value decreasing to the extent where IB-Disjoint's performance reaches that of the IB-GP. For less constrained models, IB-Disjoint surpasses IB-GP (refer to Appendix 5). Interestingly, IB-GP achieves good neural prediction performance for the Natural dataset even with two latents. For the Brownian dataset, IB-GP keeps its performance gap with IB-Disjoint even for a large number of latents. This is due to the strong correlation between the Brownian stimuli dataset (refer to Appendix 4 to observe some examples of stimuli). Both IB-GP and IB-Disjoint outperform the Feedforward CNN when a sufficient number of latents are used (4 latents and $\beta < 0.033$) for Natural and (27 latents and $\beta < 0.01$) for the Brownian dataset.

Comparison of the IB-GP and IB-Disjoint learned dynamics In Figure 3, we analyze the learned dynamics of the IB-GP and IB-Disjoint trained under the same conditions on the Natural dataset

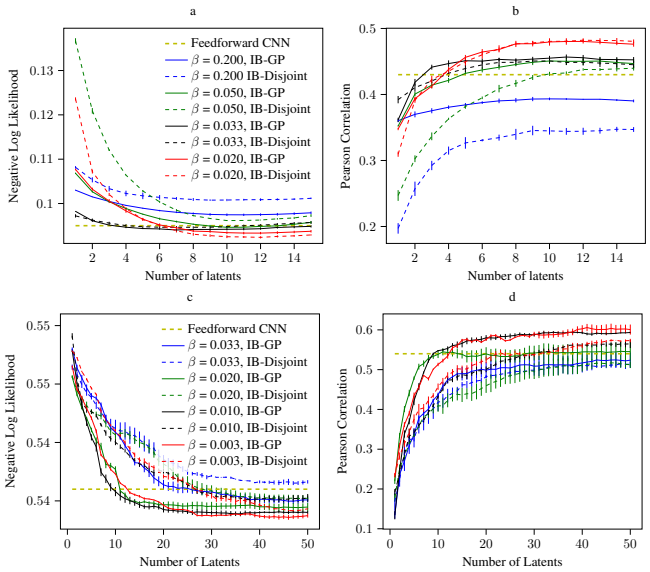

Figure 2: Overview of the RGCs' neural activity prediction accuracy for the IB-GP, IB-Disjoint, and Feedforward CNN trained on the Natural and Brownian dataset. (a) Poisson negative log-likelihood of the predicted neural responses and (b) Pearson correlation of the predicted and true spike responses as a function of the number of latents for different values of the prior pressure constraint β for the Natural dataset. (c, d) the same as (a,b) but for the Brownian dataset.

(results for the Brownian dataset are in Appendix 7). For $\beta = 0.05$ and 15 latents, performances of the IB-GP and IB-Disjoint in prediction of RGCs responses are similar (correlation ~ 0.45 vs. ~ 0.43, respectively). Nevertheless, the amount of information picked by latents in each model varies significantly. To show this, we perform a traversal analysis of the latents and report the variability in the output responses for each traversed latent in Figure 3(a,d). The KL divergence for each latent is also plotted. As observed in the figure, IB-GP lumps most of the information required to explain the neural responses in one factor. In comparison, this information is spread over five factors in IB-Disjoint. Analyzing the dynamics of the latents in each model can provide further insight. Figure 3(b,e) visualizes the inferred dynamics of the most informative latent in each model after reducing the dimension to 2 with T-SNE. As observed in the figure, the dynamics of the most informative latent in the IB-GP have 10 clusters. Strikingly, these ten clusters correspond to the ten unique stimuli in the dataset. We note that each batch of data in the Natural dataset contains 1000 consecutive images. Every 100 images are in fact, one unique image that is jittered and displayed on the retina. Auto-Correlation (AC) plots of the latents corroborate these findings. As evident from Figure 3(c,f), AC of the most informative latent in the IB-GP closely follows the statistics of the true and predicted responses of the model (averaged over all neurons). While the AC of the IB-Disjoint's predicted responses is similar to that of the true responses, the AC of its latents is very different. To demonstrate the efficacy of the IB-GP model in fitting the RGCs responses, neural activity predictions of both models are shown in Figure 3 (g,h). Refer to Appendix 8 for a more detailed interpretation of IB-GP's latent dynamics.

6.2 Closed loop image synthesis

Figure 4 reports the training results of the closed-loop experiment after the first round of measurements. Both the IB-GP and IB-Disjoint are used as the forward model in the training of the image synthesizer. We consider two scenarios when tuning the hyperparameters in the objective function of the image synthesizer. Scenario one: the image synthesizer is trained only to reduce the complexity of the original stimuli independently from the RGCs responses (equivalent to setting $\alpha = \infty$ in the objective function of the image synthesizer). In this scenario, we also consider the case where the TV smoothness constraint is dropped. These are important cases because they answer this valid question: can a simple dimensionality-reduction technique be used for synthesizing images that elicit responses correlated with the original ones? Scenario Two: the image synthesizer is trained

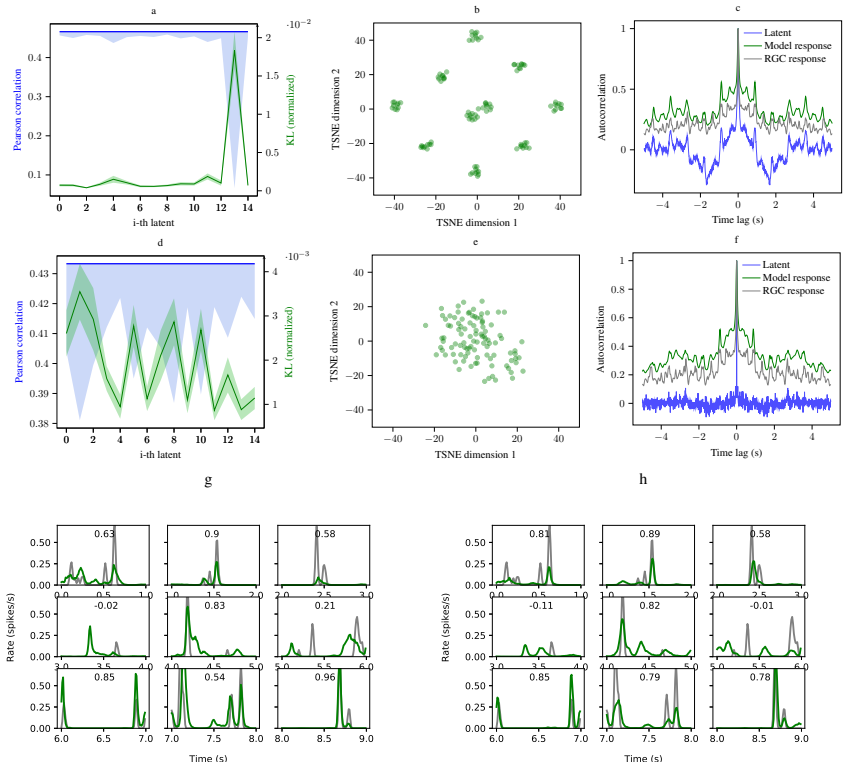

Figure 3: Analysis of the IB-GP and IB-Disjoint's learned dynamics. (a,d) The average prediction accuracy of the IB-GP and IB-Disjoint, measured by the Pearson correlation, is shown as a flat line. The variability in the accuracy of the model for traversed latent factors is depicted as blue shades. Averaged normalized KL divergence of each latent is also plotted. (b,e) The inferred dynamics of the most informative latent variable from (a,d) are visualized after reducing the dimensions to 2 with T-SNE. (c,f) AC of the most informative latent is compared against those of the true temporal activity and the model's predicted responses. (g,h) Neural activity prediction of the models. Numbers show the correlation of the predicted responses with the true activities.

in conjunction with RGCs responses ($\alpha \neq 0$). Figure 4(a, b) plot the Pearson correlation and negative log-likelihood of the RGCs responses predicted by the true model in response to the stimuli obtained by the image synthesizer network for the two scenarios. The TV loss of the obtained synthesized stimuli in each case is plotted in Figure 4c . As can be observed in the Figure 4d, dimensionality reduction of the stimuli without neural information results in non-smoothed images (column 4) or smoothed images (column 5) but poor RGC response accuracy (rightmost results in Fig. 4a-c). On the contrary, incorporating RGC neural information obtains synthesized stimuli with excellent smoothness and significant RGC response accuracy (Fig. 4a-c and column 2 in F4d). These results demonstrate the robustness of the proposed algorithm in finding synthesized images that provide accurate responses. Strikingly, when IB-GP is used as the forward model in the closed-loop experiment, complex curvature shapes appear in the synthesized images. Expectedly, these shapes appear where the neurons' receptive field is located. The receptive fields (RFs) of the neurons, obtained by Spike-triggered Average (STA) analysis [1], are also shown in the figure. Finally, we continue the optimization of the image synthesizer for the IB-GP model with hyperparameter $\alpha = 0.1$ for another two rounds. The Pearson correlation of the synthesized stimuli in all three rounds reads as: 0.353, 0.366, and 0.361. Details of the iterative optimization and evolution of the synthesized images in each phase are explained in Appendix 9. The last row in the Figure 4d shows a failure mode of the image synthesizer algorithm. We tested the image synthesizer (trained on the Natural dataset) on the white noise data. As seen from the figure, IB-Disjoint provides a superior synthesized image than other methods. This is in line with our observations that the IB-GP model fails to fit neural data elicited by white noise. More results are available in Appendix 10.

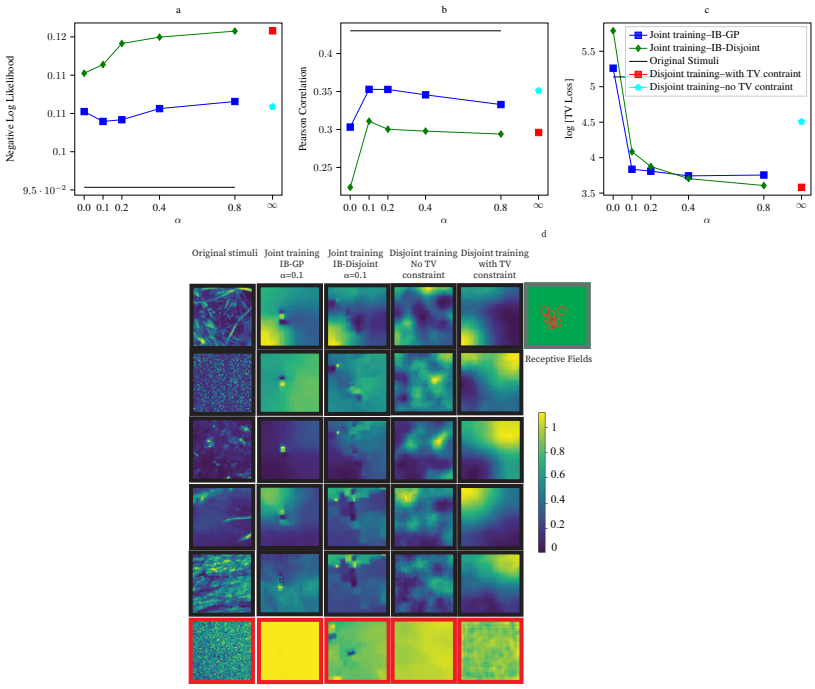

Figure 4: Summary of the closed-loop image synthesis experiment. The image synthesizer is trained either with the forward model (joint training) or without the forward model in the loop (disjoint training). We used both the IB-GP and IB-Disjoint as the forward model in the former case. In the latter case, the synthesizer is trained only to reconstruct the high-dimensional stimuli without incorporating any information from RGCs. The disjoint training is either subject to a smoothness constraint on the reconstructed images or with no constraint. (a) Poisson negative log-likelihood and (b) Pearson correlation for the RGC neural activity predictions. (c) TV loss for the synthesized stimuli. Performances of the original stimuli in the true model are depicted as a flat black line. Joint training with IB-GP with $\alpha = 0.1$ as the forward model achieves the best performance among all cases. (d) Examples of the synthesized images in all scenarios. IB-GP synthesized images contain particular patterns that are within the RFs of cells. The RFs of the neurons are depicted at scale.

7 Discussion

This work presents the IB-GP model, a latent space variational model that learns a low-dimensional representation of the Natural stimuli and RGCs responses. We observed that the IB formulation of the neural activity fitting allows learning of a low-dimensional representation of the stimuli and RGC responses which is more predictive than the feedforward models. We demonstrated that incorporating a temporal prior on the latent space of the IB model factorizes the sources of neural variability into fewer latents. The Latent analysis of the model revealed the superior performance of the IB-GP to IB-Disjoint, a variation of the proposed model with no temporal prior on the latents. The proposed model was then used in a closed-loop experiment to synthesize input stimuli that, while of lower complexity, elicit neuronal responses as those elicited by the original complex stimuli. Given the promising results demonstrating the usefulness of the model, the IB-GP model has some limitations too. First, it is unclear what type of temporal prior is sufficient for the best factorization of latents. Although the Cauchy kernel has proved efficient in modeling multi-scale dynamics [13], it might be that other temporal kernels, a combination of several kernels, or even spatio -temporal kernels [9] could improve disentangling of the latents. Second, we observed the failure mode of the IB-GP model in the fitting of the white noise stimuli due to the lack of temporal correlation. Accordingly, the IB-GP model could be modified to work for all types of stimuli. Third, computing the covariances of the IB-GP prior is computationally intensive, especially for the long temporal datasets. This might also be a possible negative societal impact of our work, resulting in a large carbon footprint.

References

[1] J. Ahn, B. Rueckauer, Y. Yoo, and Y. S. Goo. New features of receptive fields in mouse retina through spike-triggered covariance. *Experimental Neurobiology*, 29(1):38, 2020.

[2] A. A. Alemi, I. Fischer, J. V. Dillon, and K. Murphy. Deep variational information bottleneck. *arXiv preprint arXiv:1612.00410*, 2016.

[3] R. Bamler and S. Mandt. Structured black box variational inference for latent time series models. *arXiv preprint arXiv:1707.01069*, 2017.

[4] P. Bashivan, K. Kar, and J. J. DiCarlo. Neural population control via deep image synthesis. *Science*, 364(6439), 2019.

[5] E. Batty, J. Merel, N. Brackbill, A. Heitman, A. Sher, A. Litke, E. Chichilnisky, and L. Paninski. Multilayer recurrent network models of primate retinal ganglion cell responses. 2016.

[6] J. Benesty, J. Chen, Y. Huang, and I. Cohen. Pearson correlation coefficient. In *Noise reduction in speech processing*, pages 1–4. Springer, 2009.

[7] D. M. Blei and J. D. Lafferty. Dynamic topic models. In *Proceedings of the 23rd international conference on Machine learning*, pages 113–120, 2006.

[8] V. Botella-Soler, S. Deny, G. Martius, O. Marre, and G. Tkačik. Nonlinear decoding of a complex movie from the mammalian retina. *PLoS computational biology*, 14(5):e1006057, 2018.

[9] F. P. Casale, A. V. Dalca, L. Saglietti, J. Listgarten, and N. Fusi. Gaussian process prior variational autoencoders. *arXiv preprint arXiv:1810.11738*, 2018.

[10] A. Chambolle, V. Caselles, D. Cremers, M. Novaga, and T. Pock. An introduction to total variation for image analysis. *Theoretical foundations and numerical methods for sparse recovery*, 9(263-340):227, 2010.

[11] E. Chichilnisky. A simple white noise analysis of neuronal light responses. *Network: computation in neural systems*, 12(2):199, 2001.

[12] G. F. Elsayed and J. P. Cunningham. Structure in neural population recordings: an expected byproduct of simpler phenomena? *Nature neuroscience*, 20(9):1310–1318, 2017.

[13] V. Fortuin, D. Baranchuk, G. Rätsch, and S. Mandt. Gp-vae: Deep probabilistic time series imputation. In *International conference on artificial intelligence and statistics*, pages 1651–1661. PMLR, 2020.

[14] J. A. Gallego, M. G. Perich, L. E. Miller, and S. A. Solla. Neural manifolds for the control of movement. *Neuron*, 94(5):978–984, 2017.

[15] D. Ghezzi, M. R. Antognazza, R. Maccarone, S. Bellani, E. Lanzarini, N. Martino, M. Mete, G. Pertile, S. Bisti, G. Lanzani, et al. A polymer optoelectronic interface restores light sensitivity in blind rat retinas. *Nature Photonics*, 7(5):400–406, 2013.

[16] M. Greschner, A. K. Heitman, G. D. Field, P. H. Li, D. Ahn, A. Sher, A. M. Litke, and E. Chichilnisky. Identification of a retinal circuit for recurrent suppression using indirect electrical imaging. *Current Biology*, 26(15):1935–1942, 2016.

[17] A. Heitman, N. Brackbill, M. Greschner, A. Sher, A. Litke, and E. Chichilnisky. Testing pseudo-linear models of responses to natural scenes in primate retina. biorxiv, 045336, 2016.

[18] I. Higgins, L. Matthey, A. Pal, C. Burgess, X. Glorot, M. Botvinick, S. Mohamed, and A. Lerchner. beta-vae: Learning basic visual concepts with a constrained variational framework. 2016.

[19] C. Hurwitz, A. Srivastava, K. Xu, J. Jude, M. Perich, L. Miller, and M. Hennig. Targeted neural dynamical modeling. *Advances in Neural Information Processing Systems*, 34, 2021.

[20] L. H. Jepson, P. Hottowy, G. A. Weiner, W. Dabrowski, A. M. Litke, and E. Chichilnisky. High-fidelity reproduction of spatiotemporal visual signals for retinal prosthesis. *Neuron*, 83(1): 87–92, 2014.

[21] I. Khemakhem, D. Kingma, R. Monti, and A. Hyvarinen. Variational autoencoders and nonlinear ica: A unifying framework. In *International Conference on Artificial Intelligence and Statistics*, pages 2207–2217. PMLR, 2020.

[22] S. Kim, S. Sadda, J. Pearlman, M. Humayun, E. de Juan Jr, B. Melia, and W. Green. Morphometric analysis of the macula in eyes with disciform age-related macular degeneration. *Retina*, 22(4):471–477, 2002.

[23] N. Maheswaranathan, L. T. McIntosh, H. Tanaka, S. Grant, D. B. Kastner, J. B. Melander, A. Nayebi, L. Brezovec, J. Wang, S. Ganguli, et al. The dynamic neural code of the retina for natural scenes. *BioRxiv*, page 340943, 2019.

[24] K. Mathieson, J. Loudin, G. Goetz, P. Huie, L. Wang, T. I. Kamins, L. Galambos, R. Smith, J. S. Harris, A. Sher, et al. Photovoltaic retinal prosthesis with high pixel density. *Nature photonics*, 6(6):391–397, 2012.

[25] L. McIntosh, N. Maheswaranathan, A. Nayebi, S. Ganguli, and S. Baccus. Deep learning models of the retinal response to natural scenes. *Advances in neural information processing systems*, 29:1369–1377, 2016.

[26] S. Nirenberg and C. Pandarinath. Retinal prosthetic strategy with the capacity to restore normal vision. *Proceedings of the National Academy of Sciences*, 109(37):15012–15017, 2012.

[27] C. Pandarinath, D. J. O'Shea, J. Collins, R. Jozefowicz, S. D. Stavisky, J. C. Kao, E. M. Trautmann, M. T. Kaufman, S. I. Ryu, L. R. Hochberg, et al. Inferring single-trial neural population dynamics using sequential auto-encoders. *Nature methods*, 15(10):805–815, 2018.

[28] J. W. Pillow, L. Paninski, V. J. Uzzell, E. P. Simoncelli, and E. Chichilnisky. Prediction and decoding of retinal ganglion cell responses with a probabilistic spiking model. *Journal of Neuroscience*, 25(47):11003–11013, 2005.

[29] J. W. Pillow, J. Shlens, L. Paninski, A. Sher, A. M. Litke, E. Chichilnisky, and E. P. Simoncelli. Spatio-temporal correlations and visual signalling in a complete neuronal population. *Nature*, 454(7207):995–999, 2008.

[30] B. Rahmani, D. Loterie, E. Kakkava, N. Borhani, U. Teğin, D. Psaltis, and C. Moser. Actor neural networks for the robust control of partially measured nonlinear systems showcased for image propagation through diffuse media. *Nature Machine Intelligence*, 2(7):403–410, 2020.

[31] P. T. Sadtler, K. M. Quick, M. D. Golub, S. M. Chase, S. I. Ryu, E. C. Tyler-Kabara, B. M. Yu, and A. P. Batista. Neural constraints on learning. *Nature*, 512(7515):423–426, 2014.

[32] O. G. Sani, H. Abbaspourazad, Y. T. Wong, B. Pesaran, and M. M. Shanechi. Modeling behaviorally relevant neural dynamics enabled by preferential subspace identification. *Nature Neuroscience*, 24(1):140–149, 2021.

[33] N. Shah, S. Madugula, P. Hottowy, A. Sher, A. Litke, L. Paninski, and E. Chichilnisky. Efficient characterization of electrically evoked responses for neural interfaces. *Advances in Neural Information Processing Systems*, 32:14444–14458, 2019.

[34] N. Tishby, F. C. Pereira, and W. Bialek. The information bottleneck method. *arXiv preprint physics/0004057*, 2000.

[35] M. Tschannen, O. Bachem, and M. Lucic. Recent advances in autoencoder-based representation learning. *arXiv preprint arXiv:1812.05069*, 2018.

[36] E. Y. Walker, F. H. Sinz, E. Cobos, T. Muhammad, E. Froudarakis, P. G. Fahey, A. S. Ecker, J. Reimer, X. Pitkow, and A. S. Tolias. Inception loops discover what excites neurons most using deep predictive models. *Nature neuroscience*, 22(12):2060–2065, 2019.

[37] D. Zhou and X.-X. Wei. Learning identifiable and interpretable latent models of high-dimensional neural activity using pi-vae. *Advances in Neural Information Processing Systems*, 33:7234–7247, 2020.

[38] E. Zrenner, K. U. Bartz-Schmidt, H. Benav, D. Besch, A. Bruckmann, V.-P. Gabel, F. Gekeler, U. Greppmaier, A. Harscher, S. Kibbel, et al. Subretinal electronic chips allow blind patients to read letters and combine them to words. *Proceedings of the Royal Society B: Biological Sciences*, 278(1711):1489–1497, 2011.

Checklist

1. For all authors...
   (a) Do the main claims made in the abstract and introduction accurately reflect the paper's contributions and scope? [Yes] See section 6 1 and 2
   (b) Did you describe the limitations of your work? [Yes] See section 7
   (c) Did you discuss any potential negative societal impacts of your work? [Yes] See section 7
   (d) Have you read the ethics review guidelines and ensured that your paper conforms to them? [Yes]
2. If you are including theoretical results...
   (a) Did you state the full set of assumptions of all theoretical results? [Yes] See section 3 and Appendix 1
   (b) Did you include complete proofs of all theoretical results? [N/A]
3. If you ran experiments...
   (a) Did you include the code, data, and instructions needed to reproduce the main experimental results (either in the supplemental material or as a URL)? [Yes] See the footnote in section1 and Appendix 11
   (b) Did you specify all the training details (e.g., data splits, hyperparameters, how they were chosen)? [Yes] See section5 and Appendix 3
   (c) Did you report error bars (e.g., with respect to the random seed after running experiments multiple times)? [Yes] See section 6
   (d) Did you include the total amount of compute and the type of resources used (e.g., type of GPUs, internal cluster, or cloud provider)? [Yes] See the footnote in section1 and Appendix 11
4. If you are using existing assets (e.g., code, data, models) or curating/releasing new assets...
   (a) If your work uses existing assets, did you cite the creators? [Yes] The dataset asset are cited in section 5
   (b) Did you mention the license of the assets? [Yes] One dataset is public and the other is proprietary. See Dataset subsection in section 5
   (c) Did you include any new assets either in the supplemental material or as a URL? [No] a sample of data will be added in the supplementary material for verification purposes.
   (d) Did you discuss whether and how consent was obtained from people whose data you're using/curating? [Yes] One dataset is public. The other was provided by the authors of the cited paper. See Dataset subsection in section 5
   (e) Did you discuss whether the data you are using/curating contains personally identifiable information or offensive content? [N/A]
5. If you used crowdsourcing or conducted research with human subjects...
   (a) Did you include the full text of instructions given to participants and screenshots, if applicable? [N/A]
   (b) Did you describe any potential participant risks, with links to Institutional Review Board (IRB) approvals, if applicable? [N/A]
   (c) Did you include the estimated hourly wage paid to participants and the total amount spent on participant compensation? [N/A]